# Quantum spin Hall phase transition in the $\alpha$-$T_3$ lattice

J. Wang and Jun-Feng Liu*
*School of Physics, Southeast University, Nanjing, 210096, China*
*and School of Physics and Materials Science, Guangzhou University, Guangzhou 510006, China*

(Received 15 November 2020; accepted 1 February 2021; published 12 February 2021)

We report a theoretic study of the topological properties of the $\alpha$-$T_3$ lattice by taking the intrinsic spin orbit interaction into account. It is shown that when $0 < \alpha < 1$, the electronic band structure is spin-valley split and the original flat band is distorted to display a nonzero dispersion that imparts the system to be metallic. The gapped valence or conduction band shows the quantum spin Hall phase and experiences a topological phase transition from the spin Chern number $C_s = 1$ to $C_s = 2$ at the critical point $\alpha = \frac{1}{2}$. When a staggered magnetization order is considered in the system, a bunch of topological phases appear such as the quantum spin quantum anomalous Hall phase with variation of $\alpha$ or the magnetization strength.

DOI: 10.1103/PhysRevB.103.075419

## I. INTRODUCTION

Two-dimensional (2D) materials with band structures possessing a nontrivial topology have attracted much research interest in past decades [1–10] and one of main characteristics is that the low-energy states of these materials can be described by the massless Dirac equation [11,12]. Generally, the Dirac electrons in those materials have an extra $S = \frac{1}{2}$ lattice pseudospin degree of freedom besides the usual spin and charge degrees of freedom. Until recently, the study of the topological properties of the pseudospin-$\frac{1}{2}$ systems has been extended to the Dirac systems [13–42] with a larger pseudospin $N = (1, 3/2, \cdots)$. Similarly, those quasiparticles can also be interpreted by a pseudospin-$N$ Dirac-Weyl Hamiltonian.

The $\alpha$-$T_3$ lattice model is one of the well-known realizations of the $S = 1$ fermions in the 2D Dirac systems. This model is an interpolation between the graphene and dice lattices [15], the AB atoms consist in the honeycomb lattice while a hub C atom sits in each hexagon center. This special lattice structure leads to three energy bands such as two Dirac cones together with a flat band in Fig. 1. The $\alpha$-$T_3$ model can retrieve to the graphene lattice at $\alpha = 0$ and represent the dice one when $\alpha = 1$. The dice lattice can naturally be built by growing trilayers of cubic superlattices (e.g., $SrTiO_3/SrIrO_3/SrTiO_3$) in the (111) direction [19]. The optical dice lattice [20] was also suggested to be generated in theory by interfering three counterpropagating pairs of identical laser beams on a plane with the same wavelength. By dephasing one pair of the laser beams while keeping other parameters unaltered [21], the optical $\alpha$-$T_3$ lattice was successfully simulated and the parameter $\alpha$ can be varied. It has been recently demonstrated that the $Hg_{1-x}Cd_xTe$ [22] at a critical doping could be mapped onto the $\alpha$-$T_3$ model with an intermediate parameter $\alpha = 1/\sqrt{3}$.

The $\alpha$-$T_3$ model has two prominent characteristics, one is the dispersionless flat band and the other is the $\alpha$-dependent Berry phase of the electrons. It is generally believed that these two features can exert a huge effect on the material properties and functions. Many unconventional physics phenomena have been demonstrated such as the unconventional quantum Hall effect [23–25], super-Klein-tunneling [13,26,27], supercollimation phenomenon [28]. Some other exotic results have also been revealed including the diffraction-free wave propagation and novel conical diffraction [29–32], unconventional Anderson localization [33–36], flat-band ferromagnetism [37], unusual Landau-Zener Bloch oscillations [38], and peculiar magnetic-optical effect [39–41]

The possible topological phase of the $\alpha$-$T_3$ model is also one of the most intriguing subjects. Very early, Wang and Ran [42] pointed out the possibility of a nearly flat band with Chern number $C = 2$ on the dice lattice by taking Rashba spin orbit interaction into account together with ferromagnetism that splits the flat band. The introduction of the Coulomb interaction of electrons instead of the magnetization has recently been investigated by Soni *et al.* [43] in the $\alpha$-$T_3$ nanorribbon system and a similar conclusion was achieved. For $0 < \alpha < 1$, the study of the $\alpha$-$T_3$ topology with variation of $\alpha$ are relatively few and most of them were focusing on the possible optically irritated Floquet topological phase [44–53]. For instance, Dey and Ghosh [44] found that the off-resonant circularly polarized radiation upon the $\alpha$-$T_3$ lattice plane can make it experiencing a topological phase transition at $\alpha = 1/\sqrt{2}$ from $C = 1$ to $C = 2$, which is independent of the radiation amplitude. Since the intrinsic spin orbit interaction (SOI) introduced in graphene by Kane and Mele [54], the quantum spin Hall insulator (QSH) has sparked a huge interest in the topology study. Therefore, it is desirable to investigate how the intrinsic SOI changes the possible topology of the $\alpha$-$T_3$ model in theory, especially with variation of $\alpha$.

In this work, we show that the SOI in the $\alpha$-$T_3$ model will make the spin-valley splitting of the band structures and the original flat band without the SOI is distorted to exhibit

*phjfliu@gzhu.edu.cn

 

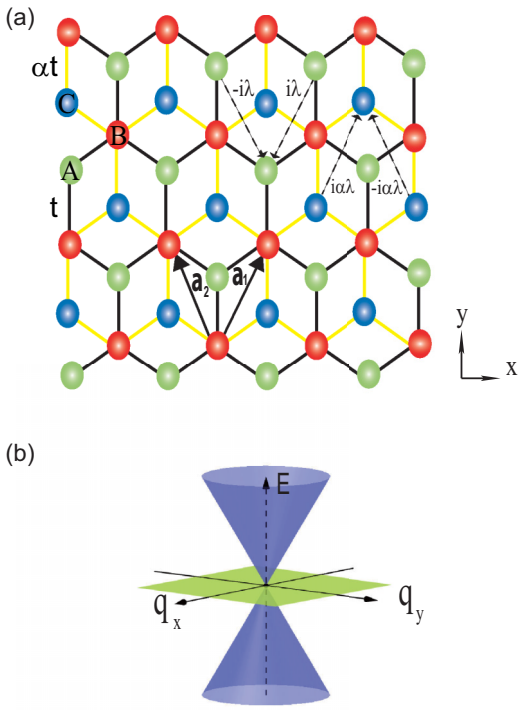


FIG. 1. (a) The lattice structure of the $\alpha$-$T_3$ lattice, where A and B sites constitute the original honeycomb lattice while the C site resides in each hexagon center. $\mathbf{a}_1$ and $\mathbf{a}_2$ are the unit vectors of the lattice. The dashed arrows represent the hopping among the next nearest neighboring atoms such as A-B-A or C-B-C to describe the intrinsic SOI. (b) A single-valley energy spectrum of Dirac particles in the $\alpha$-$T_3$ lattice. A flat band sits at the crossing point of the two Dirac cones.

a nonzero dispersion, which imparts metallic character to the system. This is exactly opposite to the graphene case, which transforms from the semimetallic phase to the insulating phases. For the gapped conduction and valence bands, they have a nonzero spin Chern number that can suddenly transfer from $C_s = 1$ to $C_s = 2$ at the critical point of $\alpha = 1/2$ indicating a topological phase transition. When a staggered magnetization is introduced into the lattice, several topological phases are induced with variation of the parameter $\alpha$ or the magnetization strength $M$ such as the quantum spin quantum anomalous Hall phase (QSQAH).

This work is organized as follows. In Sec. II, we introduce an $\alpha$-$T_3$ lattice model and present its band structure. In Sec. III, we discuss the topological phase transition with variation of $\alpha$. In the Sec. IV, we study the possible topological phases by introducing a staggered magnetization into the system. A brief conclusion is drawn in the last section.

## II. MODEL AND FORMULA

The $\alpha$-$T_3$ lattice structure is schematically shown in Fig. 1(a) and it is just an interpolation [15] between the graphene ($\alpha = 0$) and dice ($\alpha = 1$) lattices, i.e., the honeycomb lattice are composed of the A and B sites while the C sites are introduced in the center of each hexagon. The parameter $\alpha$ is manifested in the hopping energy between the site B and C, $t' = \alpha t$, where $t$ is the hopping energy between the A and B sites of the graphene lattice, the hopping between the A and C sites is prohibited. Including the intrinsic SOI, the $\alpha$-$T_3$ lattice Hamiltonian is given by

$$\mathcal{H} = \sum_{\langle ij\rangle} t c^\dagger_{i\sigma} c_{j\sigma} + \sum_{\langle jk\rangle} t' c^\dagger_{j\sigma} c_{k\sigma} + \frac{i\lambda}{3\sqrt{3}} \sum_{\langle\langle ij\rangle\rangle\sigma\sigma'} \nu_{ij} C^\dagger_{i\sigma} \sigma_z C_{j\sigma'} + \frac{i\lambda'}{3\sqrt{3}} \sum_{\langle\langle jk\rangle\rangle\sigma\sigma'} \nu_{kj} C^\dagger_{j\sigma} \sigma_z C_{k\sigma'}, \quad (1)$$

where $c^\dagger_{i,j,k}$ ($c_{i,j,k}$) is the creation (annihilation) operator of electrons on the corresponding A, B, and C sites denoted by $\gamma = i, j, k$ indices, respectively. The first term is the electron hopping between the A and B sites while the second one is that between the B and C sites. The summation of $\langle ij\rangle$ ($\langle jk\rangle$) runs over the nearest neighbor sites of AB (BC). The third term is the next nearest neighboring (NNN) hopping of electrons $\langle\langle ij\rangle\rangle$ between A and B representing the SOI proposed by Kane and Mele in graphene [54], $\lambda$ is the SOI strength. $\nu_{ij}(\nu_{kj}) = 1$ if the NNN hopping is anticlockwise and $\nu_{ij}(\nu_{kj}) = -1$ if it is clockwise with respect to the positive $z$ axis (which is perpendicular to the lattice $xy$ plane), $\sigma_z$, $\sigma$, and $\sigma'$ are the real spin Pauli operators. The last term describes the extra SOI due to the introduction of the hub C atoms into graphene lattice, i.e., the C-B-C and B-C-B NNN hoppings are feasible (A-C-A is neglected). $\lambda'$ is the corresponding SOI strength and set as $\lambda' = \alpha\lambda$ in this work for simplicity just like $t' = \alpha t$. Such an assumption of the SOI will naturally lead to the QSH phase for the $\alpha = 0$ (graphene) case.

Besides the group theoretical arguments that can present the intrinsic SOI [54], one can also obtain it by considering the intra-atomic (local atomic) spin-orbit coupling [55,56] as well as the contribution from both the $\sigma$ and $\pi$ bands. However, the later can lead to the intrinsic SOI much weaker than the Rashba SOI in the planar graphene system. In the studied $\alpha$-$T_3$ model, the lattice is not in principle planar so that the intrinsic SOI may be enhanced significantly as argued in graphene when there are corrugations/ripples or when the $\sigma$ orbit is activated to contribute to the SOI.

In the Bloch representation, the above lattice version of Hamiltonian can be transformed into a continuum one as

$$H(\sigma) = \begin{pmatrix} 0 & -tf(\mathbf{k}) & 0 \\ -tf^*(\mathbf{k}) & 0 & -t'f(\mathbf{k}) \\ 0 & -t'f^*(\mathbf{k}) & 0 \end{pmatrix} + \frac{2\sigma \mathrm{Im}[f_0(\mathbf{k})]}{3\sqrt{3}} \begin{pmatrix} -\lambda & 0 & 0 \\ 0 & \lambda - \lambda' & 0 \\ 0 & 0 & \lambda' \end{pmatrix}, \quad (2)$$

where $f_0(\mathbf{k}) = e^{i\mathbf{k}\cdot\mathbf{a}_1} - e^{i\mathbf{k}\cdot\mathbf{a}_2} - e^{i\mathbf{k}\cdot(\mathbf{a}_1-\mathbf{a}_2)}$, $f(\mathbf{k}) = 1 + e^{-i\mathbf{k}\cdot\mathbf{a}_1} + e^{-i\mathbf{k}\cdot\mathbf{a}_2}$ with $\mathbf{a}_1 = (1/2, \sqrt{3}/2)a$ and $\mathbf{a}_2 = (-1/2, \sqrt{3}/2)a$ being the lattice unit vector marked in the Fig. 1(a), $a$ is the lattice constant. $\sigma = \pm 1 = \uparrow (\downarrow)$ denotes the two spin eigenvalues, as a matter of fact, the $z$ axis is taken as the quantum spin axis. The diagonal term is the SOI that can lift the triplet degeneracy of the semimetallic point. Without SOI, the band structure comprises a dispersionless flat band ($E = 0$) flanked

by two dispersive bands: $E = \pm t|f(\mathbf{k})|$, i.e., the conduction and valence bands (Dirac cones) touch with each other at the point where the flat band is crossing. The touching points of the three bands with spin-1 Dirac-Weyl dispersion are exactly at the Brillouin zone $K$ and $K'$ called Dirac points. The low-energy excitations around these points are governed by a pseudospin-1 Dirac-Weyl Hamiltonian, which reads

$$H(\mathbf{q}) = \hbar v_f \begin{pmatrix} 0 & (q_x\eta - iq_y)\cos\theta & 0 \\ (q_x\eta + iq_y)\cos\theta & 0 & (q_x\eta - iq_y)\sin\theta \\ 0 & (q_x\eta + iq_y)\sin\theta & 0 \end{pmatrix} + \tilde{\lambda}\sigma\eta \begin{pmatrix} \cos\theta & 0 & 0 \\ 0 & \sin\theta - \cos\theta & 0 \\ 0 & 0 & -\sin\theta \end{pmatrix}, \quad (3)$$

where $\tan\theta = \alpha$, $\mathbf{q} = (q_x, q_y) = \mathbf{k} - \mathbf{K}$ or $\mathbf{k} - \mathbf{K}'$, $\eta = \pm 1 = K(K')$ representing the $K(K')$ valley, $\hbar v_f = \sqrt{3}at/2\cos\theta$, $\tilde{\lambda} = \lambda/\cos\theta$. while $\sigma$ represents the real spin degree of freedom. Here, $\alpha$ is set as $0 \leqslant \alpha \leqslant 1$, so $1 \geqslant \cos\theta \geqslant 1/\sqrt{2}$. The eigenvalues can be directly worked out as ($\hbar v_f = 1$)

$$E_{\eta\sigma}(m) = 2\sqrt{\frac{-p}{3}}\cos\left(\frac{1}{3}\cos^{-1}\left(\frac{-3\sqrt{3}q}{2\sqrt{-p^3}}\right) - \frac{2\pi(m-1)}{3}\right), (m = 1, 0, -1) \quad (4)$$

with

$$p = \tilde{\lambda}^2\sin 2\theta/2 - q^2 - \tilde{\lambda}^2 \quad (5)$$

and

$$q = (\tilde{\lambda}^2 + q^2)\tilde{\lambda}\eta\sigma\sin 2\theta(\cos\theta - \sin\theta)/2, \quad (6)$$

where $m = 1, 0, -1$ represent the conduction band, flat band, and valence band, respectively. The requirement of the above eigenvalue solution is $|\frac{-3\sqrt{3}q}{2\sqrt{-p^3}}| \leqslant 1$. The corresponding unnormalized spinor eigenfunctions are given by

$$\Psi_{\eta\sigma}(m) = \begin{pmatrix} \frac{\cos\theta(q_x - iq_y)}{E_{\eta\sigma}(m) + \sigma\eta\tilde{\lambda}\cos\theta} \\ 1 \\ \frac{\cos\theta(q_x + iq_y)}{E_{\eta\sigma}(m) - \sigma\eta\tilde{\lambda}\sin\theta} \end{pmatrix}. \quad (7)$$

When there is no SOI, $\tilde{\lambda} = 0$, the above eigenvalue can be directly simplified as $E_{\eta\sigma} = \pm\hbar v_f|\mathbf{q}|$ and 0. When $\tilde{\lambda} \neq 0$, the three electron bands would be gapped out. The energy dispersions around Dirac points ($K$ or $K'$) are plotted in Fig. 2, where only the $E$-$q_x$ ($q_y = 0$) dependence is presented because the energy band is isotropic in the moment space ($q_x$, $q_y$).

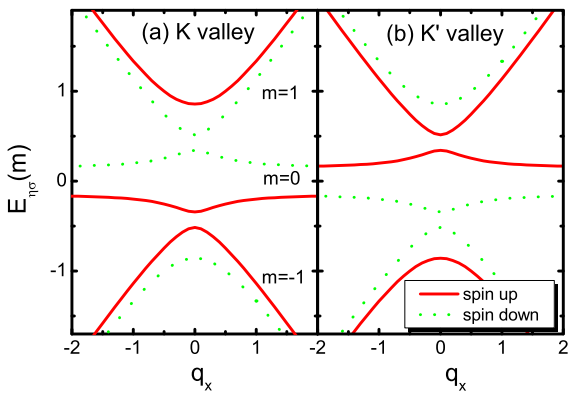


FIG. 2. Spin-resolved band structures $E_{\eta\sigma}(m)$-$q_x$ of the continuum $\alpha$-$T_3$ model for the (a) $K$ valley and (b) $K'$ valley. $m = 1, 0, -1$ denotes the conduction band, dispersive flat band, and valence band. $\tilde{\lambda} = 1$ is taken as the energy unit, $\alpha = 0.4$, and $\hbar v_f = 1$.

The $K$-valley energy dispersion ($E$-$q_x$) is shown in Fig. 2(a) and the opposite $K'$-valley situation is presented in Fig. 2(b). It is seen that the three bands are gapped with each other clearly. For $m = 0$, the original flat band [Fig. 1(b)] is now distorted, i.e., a nonzero group velocity is associated with the $m = 0$ band electrons, which will contribute to the transport properties of the system. Moreover, the $m = 0$ band shifts from the band center $E = 0$ and the opposite spin-species bands move oppositely (see, dotted and solid lines in each panel), i.e., the band is spin polarized. However, the spin polarizations are opposite again for the $K$ and $K'$ valleys. This certainly implies that the time-reversal symmetry should remain unchanged. The spin-valley splitting of the $\alpha$-$T_3$ band structure is similar to that of the TMS materials such as the $MoS_2$ [57], where the two valleys possess the opposite spin splitting but the whole system fulfills time-reversal symmetry. The spin-valley-dependent band structures will be experimentally observable by spin-valley selective circular dichroism [58], which is a phenomena that the response of the left- and right-handed circularly polarized light is different. For the graphene ($\alpha = 0$) or dice cases ($\alpha = 1$), the energy band keeps spin and valley degenerate $E_{\eta\sigma} = E_{\bar{\eta}\bar{\sigma}}$ with $\bar{\sigma} = -\sigma$ and $\bar{\eta} = -\sigma$ from Eq. (4), because the particle-hole symmetry remains invariant although the inversion symmetry is broken.

In Fig. 3, we present the evolution of the energy band with an increase of $\alpha$ since it can significantly modify the band structure. In Fig. 3(a), the $m = 0$ band shows no dispersion at $\alpha = 0$ but its dispersion grows up with $\alpha$ in Figs. 3(b) and 3(c). In Fig. 3(d) where $\alpha = 0.5$, the distorted flat band is now connecting with the valence band by closing the gap between them. With a further increase of $\alpha$, the closed gap is open again in Fig. 3(e) where $\alpha = 0.6$. For the $\alpha = 1$ case, the opened gap becomes maximum and the distorted flat band recovers to be flat again without any dispersion. Here, only the spin-up and $K$-valley ($E_{K\uparrow}$) band structure is plotted but the

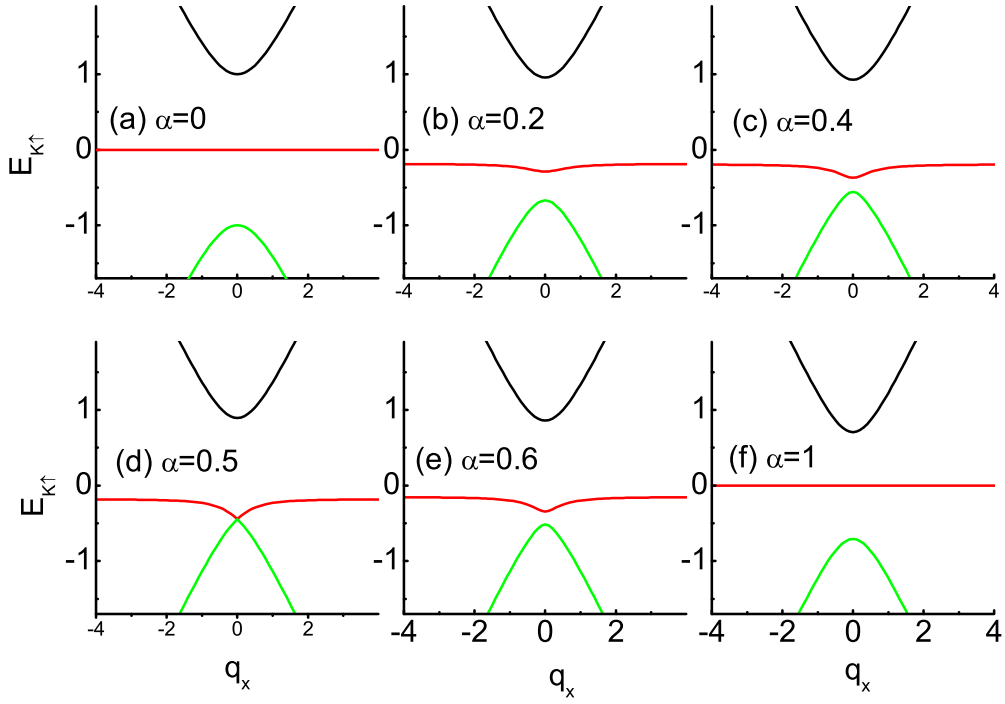


FIG. 3. Evolution of the spin-up and $K$-valley energy dispersion ($E_{K\uparrow}$) of the $\alpha$-$T_3$ with $\alpha$. Different panels correspond to different parameter of $\alpha$. Other parameters are the same those in Fig. 2.

others are essentially the same. However, the gap closure and reopening phenomenon may occur between the conduction ($m = 1$) and distorted flat ($m = 0$) bands. The critical point of $\alpha_c = \frac{1}{2}$ keeps the same and it can be directly found from the equation $E_{\eta\sigma}(-1) = E_{\eta\sigma}(0)$ or $E_{\eta\sigma}(1) = E_{\eta\sigma}(0)$.

### III. TOPOLOGICAL PHASE TRANSITION

The energy-band evolution in Fig. 3 directly suggests that there should exist a topological phase transition at $\alpha = \alpha_c$, because for $\alpha = 0$, the model is recovered to the Kane-Mele QSH insulator [54] with a spin Chern-number $C_s = 1$, while the dice lattice shows a large Chern number $C = 2$ for $\alpha = 1$ when a Haldane term was considered [51]. In order to confirm such a phase transition, one need calculate the following the spin- and valley-resolved Chern number as

$$C^m_{\eta\sigma} = \frac{1}{2\pi}\int_{BZ} d^2q\,\Omega^m_{\eta\sigma}(q), \tag{8}$$

where $\Omega^m_{\eta\sigma}$ is the Berry curvature and given by

$$\Omega^m_{\eta\sigma}(\mathbf{q}) = -i\sum_{m'\neq m}\frac{\langle\Psi_{\eta\sigma}(m)|v_x|\Psi_{\eta\sigma}(m')\rangle\langle\Psi_{\eta\sigma}(m')|v_y|\Psi_{\eta\sigma}(m)\rangle - (v_x \leftrightarrow v_y)}{[E_{\eta\sigma}(m) - E_{\eta\sigma}(m')]^2}, \tag{9}$$

where $v_x = \partial H(\mathbf{q})/\partial q_x$ and $v_y = \partial H(\mathbf{q})/\partial q_y$ is the velocity operator of electrons. This formula is gauge independent and even some singularities with no definition of the wavefunction phase do not affect the integral results [49]. However, the formula suggests that the Berry curvature could be divergent when there is a band touching as it contains $E_{\eta\sigma}(m) - E_{\eta\sigma}(m')$ in the denominator of the above equation.

In Fig. 4, we plot the spin- and valley-dependent $C^m_{\eta\sigma}$ as a function of $\alpha$ for the valence band $m = -1$. It is clearly seen that there is a discontinuous jump for $C_{K\uparrow}$ and $C_{K'\downarrow}$, which are actually corresponding to the closing point of the energy gap between the $m = 0$ and $m = -1$ bands at $\alpha_c = 1/2$ in Fig. 3. The other Chern number $C_{K'\uparrow}$ and $C_{K\downarrow}$ are continuous. The situation will reverse if one calculates the Chern number of the conduction band ($m = 1$). Although the spin- and valley-dependent Chern number deviates from the half-integer, the spin Chern number $C_s$ or charge Chern number $C$ keeps an integer as shown in the Fig. 4(b) with

$$C_s = \tfrac{1}{2}(C_{K\uparrow} - C_{K\downarrow} + C_{K'\uparrow} - C_{K'\downarrow}) \tag{10}$$

and

$$C = (C_{K\uparrow} + C_{K\downarrow} + C_{K'\uparrow} + C_{K'\downarrow}). \tag{11}$$

It is clearly shown that there is a phase transition at $\alpha_c$ from $C_s = 1$ for $\alpha < \alpha_c$ to $C_s = 2$ for $\alpha > \alpha_c$. Meanwhile, the total charge Chern number is zero. This denotes that a pair of helical edge states ($C_s = 1$) flow along the boundary of the sample for $\alpha < \alpha_c$ but two pairs of helical edges for $\alpha > \alpha_c$ and $C_s = 2$.

Since the bulk-boundary correspondence is a typical characteristic of a topological phase, we present the energy band of a nanoribbon system with open boundaries along the

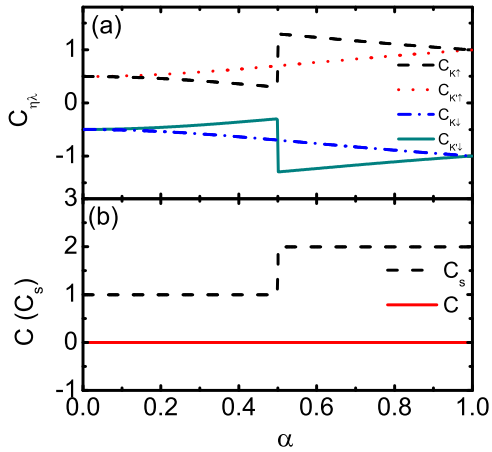


FIG. 4. Chern number of the $m = -1$ valence band as a function of $\alpha$ with the (a) spin and valley resolved one and (b) total spin or charge Chern number.

transverse direction (say, the $y$ axis) in Fig. 5. For the $\alpha < \alpha_c$ case in Fig. 5(a), four lines across the energy gap (e.g., between the $m = 0$ and $m = -1$ bands) with two spin-up green curves and two spin-down red solid ones, describe a pair of helical edges state flowing along the up and down opposite boundaries of the ribbon system. As $\alpha > \alpha_c$, the crossing lines in the same energy gap are doubled in Fig. 5(b). This implies that the two pairs of helical states flowing in each boundary of the ribbon, so $C_s = 2$ can make sense and is same as those $C = 2$ phases in the dice system [51] within the broken time-reversal symmetry. Meanwhile, one can also

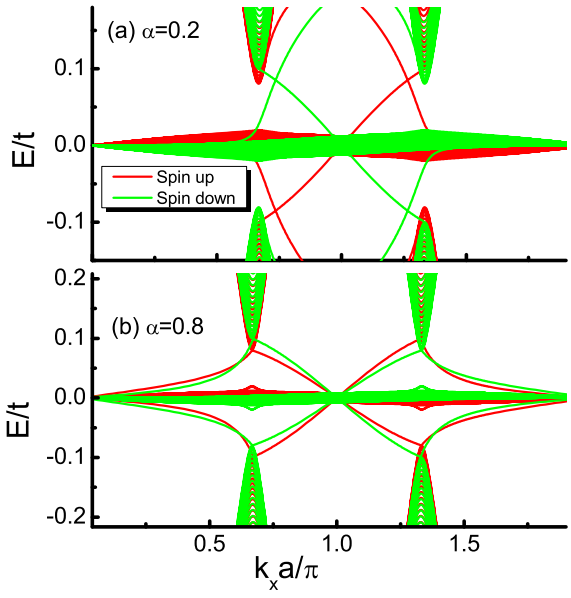


FIG. 5. (a) Spin-resolved band structures of the zigzag-type $\alpha$-$T_3$ nanoribbon for two typical cases (a) $\alpha = 0.2$ and (b) $\alpha = 0.8$. These two different $\alpha$ represent the QSHs for $C_s = 1$ and $C_s = 2$. The transverse direction of the ribbon (the $y$ axis) is open and the zigzag chain along the $y$ axis contains $N = 320$ AB sites. In the lattice calculation, $t = 1$ and $\lambda = 0.1t$.

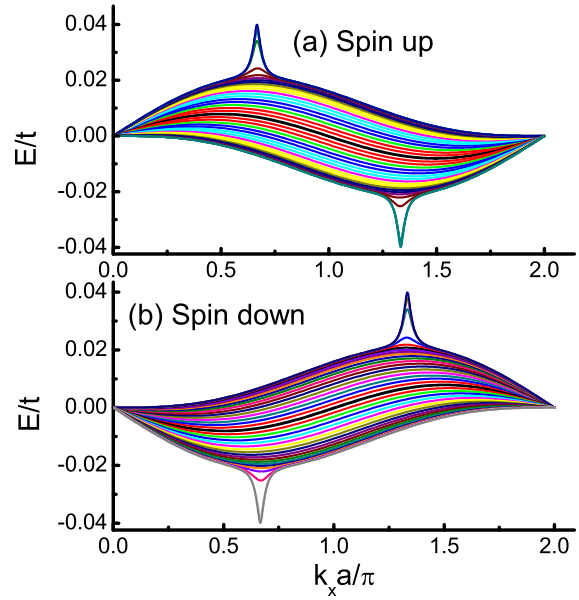


FIG. 6. (a) Spin-up and (b) spin-down band structures of the distorted flat band ($m = 0$) in the $\alpha$-$T_3$ nanoribbon system. The transverse boundaries are closed opposite to those in Fig. 5. The curves are too dense to display so that only part of them are shown. $\alpha = 0.4$, $t = 1$, and $\lambda = 0.1t$.

see that the spin and valley bands are split and the ($m = 0$) band is now distorted to show a little dispersion.

It is clearly shown that the system is actually metallic if the Fermi energy locates at the band center ($E = 0$), and the spin-resolved energy band are oppositely valley polarized crossing the band center $k_x = 0$. We enlarge the middle band ($m = 0$) and depict them in Fig. 6, where the close ribbon boundary condition is chosen in order to disappear the edge states. It is clearly shown that the energy sub-bands due to the finite-width ribbon have nonzero dispersions across the band center Γ. But the most conspicuous distortion of the original flat band locates around both the $K$ and $K'$ points. One can also directly obtain $E_\sigma$-$k_x$ relationship by diagonalizing the continuum Hamiltonian [Eq. (2)]. Figure 6 clearly shows that the system ($0 < \alpha < 1$) transforms into a metallic phase within the SOI when the Fermi energy locates still at the original charge-neutral point. This is opposite to the graphene case, which is a QSH when the intrinsic SOI is turned on [54].

## IV. TOPOLOGICAL PHASES WITH MAGNETIZATION

When $0 < \alpha < 1$, the energy band of the $\alpha$-$T_3$ lattice are spin and valley split and it is possible to get different topological phases by introducing magnetization in the system, which will break the time-reversal symmetry, so the quantum anomalous Hall effect is possible [42]. As studied in the dice lattice, the densely degenerate flat band could be spin split when the Coulomb interaction of electrons is taken into account. Here, we directly consider a simple A-C lattice staggered magnetization **M** instead of the possible magnetization from Coulomb interaction, i.e., the magnetization in A and C sites are opposite but zero in the B sites. Therefore, we should add

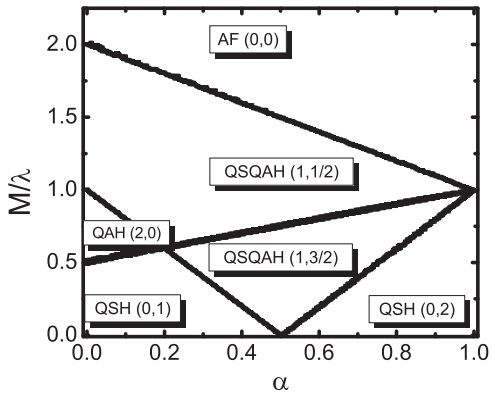


FIG. 7. Topological phase diagram $(C, C_s)$ with variation of parameter $M$ and $\alpha$. In the 2D lattice model, $t = 1$ is set as the energy unit and $\lambda = 0.1t$.

a term in the Hamiltonian of Eq. (2) as

$$H_M = M\sigma s_z = M\sigma \begin{pmatrix} 1 & 0 & 0 \\ 0 & 0 & 0 \\ 0 & 0 & -1 \end{pmatrix}, \tag{12}$$

where $s_z$ is the lattice pseudospin-$z$ component of the $S = 1$ spin operator. Note that it is assumed the magnetization keeps the same direction along the spin eigendirection of the SOI (the $z$ axis in this work). By directly diagonalizing Eq. (2) plus $H_M$ and putting the eigenfunctions into Eq. (8) for the Chern number, we can obtain spin and charge Chern number $(C, C_s)$. Here, we directly calculate the integration of Chern number in the whole Brillouin zone but not from the continuum model Eq. (3), because we do not take the two valleys independently. The corresponding phase diagram as functions of the magnetization $M$ and $\alpha$ are shown in Fig. 7, where we focus on the Chern number of the $m = -1$ valence band but the $m = 0$ flat band will be also taken into account if the valence $(m = -1)$ and flat $(m = 0)$ bands are overlapped due to nonzero $M$.

For $M = 0$, the phase diagram contains a topological phase transition at $\alpha_c = 1/2$ from (0,1) to (0,2), a pure QSH phase transition with different $C_s$, which agrees with the prediction from the continuum model in Fig. 4. For the graphene case $\alpha = 0$, the phase diagram shows that the system goes through from the QSH phase (0, 1) to the QAH phase (2,0), then to the quantum spin quantum anomalous Hall state (1,1/2), which is termed as QSQAH [59] and finally to the antiferromagnetic state (AF). The QSQAH is referred to as the phase in which one valley is the QSH state but the other valley is the QAH state. The AF state is actually a spin-resolved quantum valley Hall phase. However, the distorted flat band makes the valley definition vague and we do not discuss it here. The phases in the $\alpha = 0$ case are consistent with results in Ref. [59], where authors studied the possible topological phases in graphene by considering both the staggered magnetization $M$ and nonzero mean magnetization $\Delta M$ or inhomogeneous mass term of the Dirac electrons. For the studied $\alpha$-$T_3$ lattice, the nonzero $M$ is assumed to exist only on the A site, so there is an average magnetization $M/2$ on the AB sites when $\alpha = 0$, which is actually the inhomogeneous Dirac mass term. As a matter of fact, the spin and valley splitting from the SOI in the $\alpha$-$T_3$ band structure for $0 < \alpha < 1$ has the same origin, i.e., the

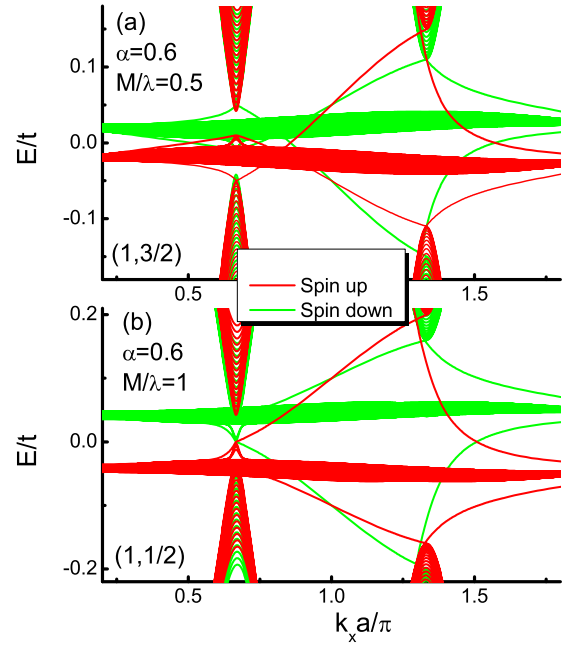


FIG. 8. Spin-resolved band structures of the zigzag-type $\alpha$-$T_3$ nanoribbon for the VPQAH phase with (a) $C_s = 3/2$ and (b) $C_s = 1/2$. Parameters are the same as those in Fig. 5.

average potential in the lattice sites is nonzero for a given spin or valley species, which leads necessarily to the original chiral symmetry broken. The interesting phase in the phase diagram of Fig. 7 is the QSQAH with the Chern number (1,3/2) in comparison with those in graphene, where only (1,1/2) is possible. We present the bulk-boundary correspondence in Fig. 8. By comparison with the QSH phase (0,2) in Fig. 4(b), Fig. 8(a) shows one spin-species edge state in one valley disappears [say, the left valley of Fig. 8(a)], as a result, a pair of helical state is replaced by the chiral state. With a further increase of $M$ in Fig. 8(b), the topological phase is given by (1,1/2), i.e., one valley is mixed with the distorted flat band and contribute to the chiral states while the opposite valley contributes to the QSH state (or helical edge state) [59].

## V. CONCLUSION

In summary, we have investigated the possible topological phases in the $\alpha$-$T_3$ lattice by considering the Kane-Mele SOI term. The electron band structures within different $\alpha$ are obtained based on a continuum model and shown to exhibit the spin-valley-dependent polarization when $0 < \alpha < 1$. The original flat band without SOI turns out to be dispersive so that the system is metallic if the Fermi energy locates at the charge neutral point. The gapped valence band or conduction band is in the quantum spin Hall phase and experiences a topological phase transition from the Chern number $C_s = 1$ phase to the $C_s = 2$ one. When a staggered magnetization is introduced in the system, several different topological phases are identified within different $\alpha$ and the magnetization strength.

## ACKNOWLEDGMENTS

The work is supported by NSFC (Grants No. 11574045 and No. 11774144).

[1] K. S. Novoselov, A. K. Geim, S. V. Morozov, D. Jiang, Y. Zhang, S. V. Dubonos, I. V. Grigorieva, and A. A. Firsov, Science **306**, 666 (2004).

[2] K. S. Novoselov, A. K. Geim, S. V. Morozov, D. Jiang, M. I. Katsnelson, I. V. Grigorieva, S. V. Dubonos, and A. A. Firsov, Nature (London) **438**, 197 (2005).

[3] M. I. Katsnelson, K. S. Novoselov, and A. K. Geim, Nature Phys. **2**, 620 (2006).

[4] A. H. Castro Neto, F. Guinea, N. M. R. Peres, K. S. Novoselov, and A. K. Geim, Rev. Mod. Phys. **81**, 109 (2009).

[5] N. M. R. Peres, Rev. Mod. Phys. **82**, 2673 (2010).

[6] S. Das Sarma, S. Adam, E. H. Hwang, and E. Rossi, Rev. Mod. Phys. **83**, 407 (2011).

[7] M. Z. Hasan and C. L. Kane, Rev. Mod. Phys. **82**, 3045 (2010).

[8] X.-L. Qi and S.-C. Zhang, Rev. Mod. Phys. **83**, 1057 (2011).

[9] X. Wan, A. M. Turner, A. Vishwanath, and S. Y. Savrasov, Phys. Rev. B **83**, 205101 (2011).

[10] K. Cai, M. Yang, H. Ju, S. Wang, Y. Ji, B. Li, K. W. Edmonds, Y. Sheng, B. Zhang, N. Zhang, S. Liu, H. Zheng, and K. Wang, Nature Mater. **16**, 712 (2017); Y. Cao, Y. Sheng, K. W. Edmonds, Y. Ji, H. Zheng, and K. Wang, Adv. Mater. **32**, 1907929 (2020).

[11] G. W. Semenoff, Phys. Rev. Lett. **53**, 2449 (1984).

[12] D. P. DiVincenzo and E. J. Mele, Phys. Rev. B **29**, 1685 (1984).

[13] Y. Betancur-Ocampo, G. Cordourier-Maruri, V. Gupta, and R. de Coss, Phys. Rev. B **96**, 024304 (2017).

[14] T. Louvet, P. Delplace, A. A. Fedorenko, and D. Carpentier, Phys. Rev. B **92**, 155116 (2015).

[15] D. F. Urban, D. Bercioux, M. Wimmer, and W. Hausler, Phys. Rev. B **84**, 115136 (2011).

[16] J. Wang, J. F. Liu, and C. S. Ting, Phys. Rev. B **101**, 205420 (2020).

[17] M. Vigh, L. Oroszlány, S. Vajna, P. San-Jose, G. Dávid, J. Cserti, and B. Dóra, Phys. Rev. B **88**, 161413(R) (2013).

[18] T. Andrijauskas, E. Anisimovas, M. Raciunas, A. Mekys, V. Kudriasov, I. B. Spielman, and G. Juzeliunas, Phys. Rev. A **92**, 033617 (2015).

[19] S. Okamoto and D. Xiao, J. Phys. Soc. Jpn. **87**, 041006 (2018).

[20] J. Vidal, R. Mosseri, and B. Doucot, Phys. Rev. Lett. **81**, 5888 (1998).

[21] A. Raoux, M. Morigi, J. N. Fuchs, F. Piechon, and G. Montambaux, Phys. Rev. Lett. **112**, 026402 (2014).

[22] J. D. Malcolm and E. J. Nicol, Phys. Rev. B **92**, 035118 (2015).

[23] E. Illes, J. P. Carbotte, and E. J. Nicol, Phys. Rev. B **92**, 245410 (2015).

[24] T. Biswas and T. K. Ghosh, J. Phys.: Condens. Matter **28**, 495302 (2016).

[25] Y. Xu and L.-M. Duan, Phys. Rev. B **96**, 155301 (2017).

[26] R. Shen, L. B. Shao, B. Wang, and D. Y. Xing, Phys. Rev. B **81**, 041410(R) (2010).

[27] E. Illes and E. J. Nicol, Phys. Rev. B **95**, 235432 (2017).

[28] A. Fang, Z. Q. Zhang, S. G. Louie, and C. T. Chan, Phys. Rev. B **93**, 035422 (2016).

[29] D. Guzmán-Silva, C. Meja-Cortés, M. Bandres, M. Rechtsman, S. Weimann, S. Nolte, M. Segev, A. Szameit, and R. Vicencio, New J. Phys. **16**, 063061 (2014).

[30] R. A. Vicencio, C. Cantillano, L. Morales-Inostroza, B. Real, C. Mejía-Cortés, S. Weimann, A. Szameit, and M. I. Molina, Phys. Rev. Lett. **114**, 245503 (2015).

[31] S. Mukherjee, A. Spracklen, D. Choudhury, N. Goldman, P. Ohberg, E. Andersson, and R. R. Thomson, Phys. Rev. Lett. **114**, 245504 (2015).

[32] F. Diebel, D. Leykam, S. Kroesen, C. Denz, and A. S. Desyatnikov, Phys. Rev. Lett. **116**, 183902 (2016).

[33] A. Fang, Z. Q. Zhang, S. G. Louie, and C. T. Chan, Proc. Natl. Acad. Sci. USA **114**, 4087 (2017).

[34] J. T. Chalker, T. S. Pickles, and P. Shukla, Phys. Rev. B **82**, 104209 (2010).

[35] J. D. Bodyfelt, D. Leykam, C. Danieli, X. Yu, and S. Flach, Phys. Rev. Lett. **113**, 236403 (2014).

[36] S. Kim and K. Kim, Phys. Rev. B **100**, 104201 (2019).

[37] S. Taie, H. Ozawa, T. Ichinose, T. Nishio, S. Nakajima, and Y. Takahashi, Sci. Adv. **1**, e1500854 (2015).

[38] R. Khomeriki and S. Flach, Phys. Rev. Lett. **116**, 245301 (2016).

[39] E. Illes and E. J. Nicol, Phys. Rev. B **94**, 125435 (2016).

[40] Y. R. Chen, Y. Xu, J. Wang, J.-F. Liu, and Z. Ma, Phys. Rev. B **99**, 045420 (2019).

[41] L. Chen, J. Zuber, Z. Ma, and C. Zhang, Phys. Rev. B **100**, 035440 (2019).

[42] F. Wang and Y. Ran, Phys. Rev. B **84**, 241103(R) (2011).

[43] R. Soni, N. Kaushal, S. Okamoto, and E. Dagotto, Phys. Rev. B **102**, 045105 (2020).

[44] B. Dey and T. K. Ghosh, Phys. Rev. B **99**, 205429 (2019).

[45] B. Dey and T. K. Ghosh, Phys. Rev. B **98**, 075422 (2018).

[46] SK. Firoz Islam and A. A. Zyuzin, Phys. Rev. B **100**, 165302 (2019).

[47] A. Iurov, G. Gumbs, and D. Huang, Phys. Rev. B **99**, 205135 (2019).

[48] M. A. Mojarro, V. G. Ibarra-Sierra, J. C. Sandoval-Santana, R. Carrillo-Bastos, and Gerardo G. Naumis, Phys. Rev. B **101**, 165305 (2020).

[49] E. V. Gorbar, V. P. Gusynin, and D. O. Oriekhov, Phys. Rev. B **99**, 155124 (2019).

[50] H. Y. Xu, L. Huang, D. Huang, and Y. C. Lai, Phys. Rev. B **96**, 045412 (2017).

[51] B. Dey, P. Kapri, O. Pal, and T. K. Ghosh, Phys. Rev. B **101**, 235406 (2020).

[52] O. Kyriienko, O. V. Kibis, and I. A. Shelykh, Phys. Rev. B **99**, 115411 (2019); O. V. Kibis, M. V. Boev, and V. M. Kovalev, *ibid.* **102**, 075412 (2020).

[53] A. Iurov, G. Gumbs, and D. Huang, J. Phys.: Condens. Matter **32**, 415303 (2020); A. Iurov, L. Zhemchuzhna, D. Dahal, G. Gumbs, and D. Huang, Phys. Rev. B **101**, 035129 (2020).

[54] C. L. Kane and E. J. Mele, Phys. Rev. Lett. **95**, 226801 (2005).

[55] D. Huertas-Hernando, F. Guinea, and A. Brataas, Phys. Rev. B **74**, 155426 (2006).

[56] H. Min, J. E. Hill, N. A. Sinitsyn, B. R. Sahu, L. Kleinman, and A. H. MacDonald, Phys. Rev. B **74**, 165310 (2006).

[57] X. Xu, W. Yao, D. Xiao, and T. F. Heinz, Nature Phys. **10**, 343 (2014).

[58] M. Ezawa, Phys. Rev. B **86**, 161407(R) (2012).

[59] M. Ezawa, Phys. Rev. B **87**, 155415 (2013).